The Journal of Experimental Biology 211, 3147-3159
Published by The Company of Biologists 2008
doi:10.1242/jeb.020263

Pitching stabilization *via* caudal fin-wave propagation in a forward-sinking parrot cichlid (*Cichlasoma citrinellum* × *Cichlasoma synspilum*)

S. C. Ting[1] and J. T. Yang[2,*]

[1]Department of Power Mechanical Engineering, National Tsing Hua University, Hsinchu, Taiwan and [2]Department of Mechanical Engineering, National Taiwan University, Taipei, Taiwan

*Author for correspondence (e-mail: jtyang@ntu.edu.tw)

Accepted 30 July 2008

SUMMARY

Caudal fin-wave propagation (CFP) is a commonly observed behavior in a fish but has been little investigated. Our objective is to understand the function of a CFP for a forward-sinking parrot cichlid that adopts a tilted-down swimming posture. We utilized stereoscopic digital particle-image velocimetry to measure the velocity fields in the wake of both the caudal fin and the pectoral fins and to evaluate the corresponding hydrodynamic forces. The tilted-down posture of this fish is inherently unstable because of the presence of the head-down pitching moment induced from the buoyant force of the body. The down-stroke of the pectoral fins results also in a head-down pitching moment that destabilizes the fish. Our results indicate that a CFP facilitates the pitching stabilization of a fish. In a forward-sinking parrot cichlid, a CFP produces periodic jets (CFP jets) that are oriented laterally and posterodorsally, which result in both thrust and negative lift that induce a head-up pitching moment. The CFP jets are initially trapped by the ventral part of the caudal fin, strengthened and reoriented by the dorsally propagating fin wave, and expelled near the dorsal part of the caudal fin.

Key words: fish, pitching stabilization, caudal fin-wave propagation, vortex, stereoscopic-DPIV, parrot cichlid.

INTRODUCTION

The shape of the caudal fin of a fish is classifiable as convex (e.g. rounded tail) or truncated (e.g. triangular or square tail) or concave (e.g. forked or lunate tail). Fish possessing convex or truncated caudal fins commonly exhibit a behavior of caudal fin-wave propagation (CFP). A caudal fin executing CFP undergoes a significant deformation because a wave of bending passes dorsally or ventrally through the fin surface (see Fig. 1).

A fish performing a CFP is typically in a hovering or slowly maneuvering state, such as forward sinking (i.e. inclined descent) or forward rising (i.e. inclined ascent). According to a reference frame on a forward-sinking fish, the CFP is observed to begin with lateral movements of the ventral edge of the caudal fin; the fin wave then forms and propagates dorsally. By contrast, during forward rising, the CFP begins with lateral movements of the dorsal edge of the caudal fin; the fin wave then forms and propagates ventrally. During hovering, both dorsal and ventral propagations of the caudal fin-wave are possible.

The propagation of a CFP is observable in a parrot cichlid that swims in still water or against a current. When a parrot cichlid initiates a forward sinking, the pectoral fins first induce a head-down pitching moment that tips the head down. Afterwards, the parrot cichlid adopts a stable tilted-down swimming posture (Fig. 1A). In this posture, the transverse amplitude (i.e. lateral displacement) of the dorsally propagating fin wave gradually increases from the ventral to the dorsal edges of the caudal fin.

The hydrostatic pitching equilibrium of a parrot cichlid is normally neutral because the centers of mass and buoyancy occur at approximately the same relative longitudinal location of the fish body. For a forward-sinking parrot cichlid that adopts a tilted-down swimming posture, however, the body should be inherently unstable in pitching as the center of buoyancy is located aft of the center of mass. The buoyant force can induce a head-down pitching moment that destabilizes the fish body but a forward-sinking parrot cichlid maintains a stable tilted-down swimming posture. The maneuvering of a forward-sinking parrot cichlid is hence related to a postural control involving pitching stabilization (Webb, 2002; Webb, 2004; Weihs, 1993). To analyze how a fish achieves this pitching stabilization, one must evaluate the hydrodynamic forces acting on the fish body, especially the longitudinal aspect (Weihs, 1993).

There has been little study CFPs. Our objective in this work has been to understand the function of a CFP in a forward-sinking parrot cichlid. We expect that the CFP is related to pitching stability. In this work, we assume that the hydrodynamic forces acting on a fish body are generated by only the caudal and pectoral fins because maneuvers of the other fins are not obvious.

Much important research has focused on the swimming hydrodynamics of heterocercal and homocercal caudal fins (Gibb et al., 1999; Lauder, 2000; Lauder and Drucker, 2002; Liao and Lauder, 2000; Müller et al., 1997; Nauen and Lauder, 2002a; Nauen and Lauder, 2002b; Stamhuis and Videler, 1995; Wilga and Lauder, 2002; Wilga and Lauder, 2004; Wolfgang et al., 1999). Wake patterns composed of linked vortex rings or a ring-within-a-ring structure were found. Some homocercal caudal fins are reported to undergo a slight deformation due to an asymmetric movement of the dorsal and ventral lobes during maneuvering, so that both thrust and lift are generated (Gibb et al., 1999; Lauder, 2000; Lauder and Drucker, 2002; Nauen and Lauder, 2002a). The heterocercal tail in sharks also produces thrust and lift (Wilga and Lauder, 2002; Wilga and Lauder, 2004). The lift generated at the tail can result in a pitching moment about the center of mass of a fish body (Weihs, 1993).

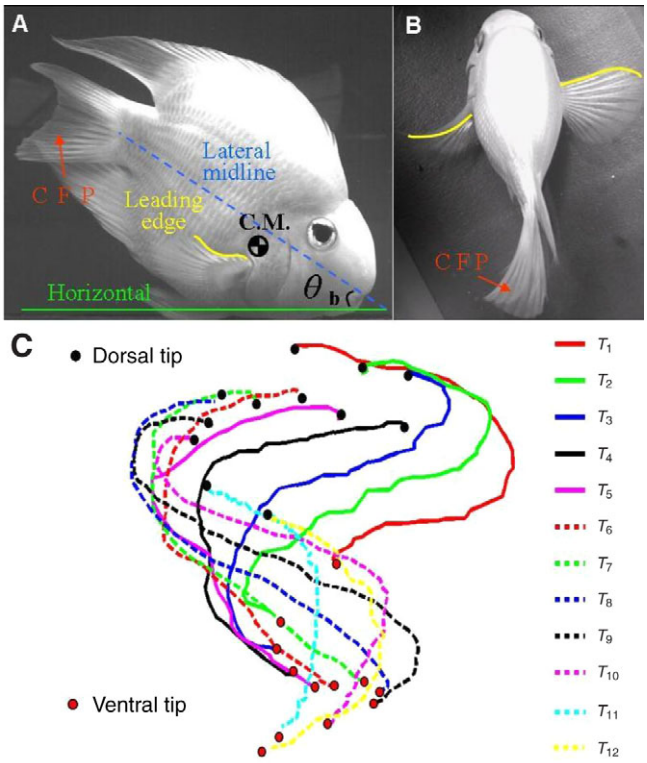

Fig. 1. A forward-sinking parrot cichlid executing a caudal fin-wave propagation (CFP). (A) Lateral view of the fish with a tilted-down swimming posture: head down and tail up. A wave of bending passes through the surface of the caudal fin. The dashed blue line indicates the lateral midline defined as a line connecting the midpoint of the peduncle base and the fish mouth. θ_b is the body angle. CM, the center of mass of the fish body, is indicated by the black and white checked circle. The yellow curved lines represent the leading edge of the pectoral fins in A and B. (B) Dorsal view of the fish. The pectoral fins are simultaneously maneuvering. (C) An example of a time series of traces of the trailing edge of the caudal fin of a parrot cichlid executing forward sinking *via* a caudal fin-wave propagation (observed from behind the fish and a laboratory-bound reference frame). These traces illustrate kinematical features of the CFP motion. T_1–T_{12} denote the time steps associated with each traces. The black and red filled circles represent the dorsal and ventral tips, respectively, of the trailing edge of the caudal fin.

The pectoral fins of a parrot cichlid invariably move while the fish is performing a CFP. For instance, as shown in Fig. 1B, the forward-sinking parrot cichlid simultaneously abducts its pectoral fin on the right side and adducts its pectoral fin on the left side. The locomotive function of pectoral fins has been investigated using kinematic analysis (Ramamurti et al., 2002; Walker and Westneat, 1997; Walker and Westneat, 2002) or wake-geometry analysis (Drucker and Lauder, 1999; Drucker and Lauder, 2000; Drucker and Lauder, 2001; Drucker and Lauder, 2003). One function of the pectoral fins is to facilitate the rolling stabilization.

In this work, we evaluated the hydrodynamic forces from the velocity fields in the fin wake, measured with stereoscopic digital particle-image velocimetry (commonly abbreviated as stereoscopic-DPIV or SDPIV). Because flow fields generated by a swimming fish are generally three-dimensional and complicated (Fish and Lauder, 2006; Müller and van Leeuwen, 2006; Tytell, 2006; Tytell et al., 2008), SDPIV is much more accurate than the traditional two-dimensional DPIV for measuring the flow velocity fields so generated (Nauen and Lauder, 2002b; Sakakibara et al., 2004). Like previous researchers (Drucker and Lauder, 1999; Drucker and Lauder, 2005; Nauen and Lauder, 2002a; Stamhuis and Nauwelaerts, 2005), we evaluated quantitatively the temporally averaged locomotive (i.e. hydrodynamic) forces based on a vortex-ring model.

MATERIALS AND METHODS

Experimental fish

Six parrot cichlids (*Cichlasoma citrinellum* × *Cichlasoma synspilum*, Günther and Hubbs) were acquired from a local distributor and housed in a laboratory aquarium (volume 288 liters, water temperature 19±2°C). Their mean (±s.d.) measurements were as follows: body length, 13.75±1.9 cm; body height, 8.52±1.87 cm; height of the caudal fin, 5.65±0.68 cm; length of the caudal fin measured from caudal peduncle to trailing edge, 4.93±0.48 cm. During the experiment, the parrot cichlid swam freely in a transparent tank filled with still fresh water; the arbitrary locomotion of a fish was its spontaneous behavior for various locomotive purposes. Accordingly, the average velocity and direction of a swimming fish were essentially variable. We therefore waited to begin recording images until a fish was in an appropriate position within the test section and swimming with a nearly steady velocity.

Stereoscopic digital particle-image velocimetry flow measurement

We used SDPIV to acquire simultaneously, on a light sheet, the in-plane and the out-of-plane velocities (U, V, W). The two SDPIV cameras (IDT X-Stream™ Vision 5 high-speed CMOS digital camera, Integrated Design Tools Inc., Taipei, Taiwan, ROC) were placed in angular type; the angles between the optical axes (i.e. viewing directions) of each camera and the light-sheet norm were 30° (Prasad, 2000). Fig. 2 shows the arrangement of the experimental apparatus for SDPIV and recording images of the fish in a Plexiglas tank (1 m×1 m×1 m; height×width×depth) filled with fresh water. The four side walls and the bottom of the tank were transparent. The beam from a CW argon-ion laser (7 W, Spectra-Physics, Stabilite 2017, Fremont, CA, USA) was expanded into a light sheet (thickness 1.5–2 mm) using cylindrical and spherical lenses. Nearly neutrally buoyant light-scattering microparticles (hollow glass spheres: specific gravity, 0.1–1.5; diameter, 8–12 µm; Potters Industries, Valley Forge, PA, USA) were seeded into the water and illuminated as tracing particles (Raffel et al., 2007). The frame rate of the two SDPIV cameras was 250 frames s^{-1}; the image resolution was 1280×1024 pixels. Particle image traces were analyzed with software (Insight version 5.0, TSI, Shoreview, MN, USA) to obtain two-dimensional DPIV velocity vectors. The procedures of DPIV correlation analysis and vector validation were similar to those described previously (Drucker and Lauder, 1999; Nauen and Lauder, 2002a; Nauen and Lauder, 2002b). The size of the interrogation window was 16×16 pixels. A Hart correlator (Insight software) was used with 50% overlap of the interrogation window. For a flow field of 10×10 cm^2, approximately 50×50 vectors were computed. The displayed vectors in the presented vector plots were adequately reduced so as not to obscure the overlapping color contours. We used backward-mapping second order polynomials to calibrate the SDPIV images (Lawson and Wu, 1997; Lecerf et al., 1999; Westerweel and Van Oord, 1999; Willert, 1997). We performed a calibration-based velocity reconstruction using TPower-SDPIV software written in Matlab (version 7.0; Mathworks, Natick, MA, USA). The measurement error of the in-plane velocity components

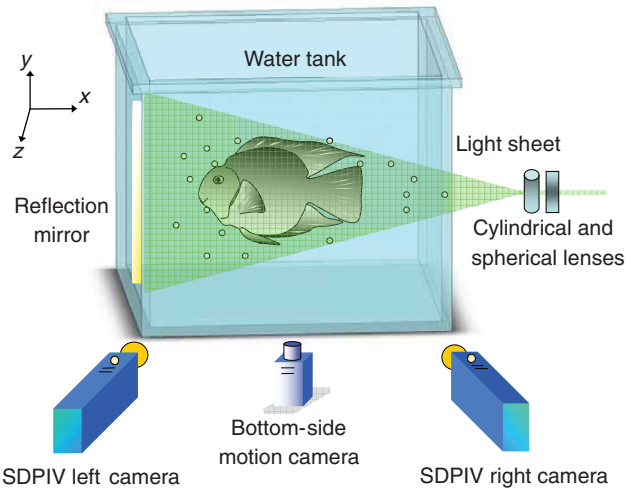

Fig. 2. Experimental apparatus for stereoscopic digital particle-image velocimetry (SDPIV) and recording images of the fish motion. This sketch shows the setup for filming the 'parasagittal' flow fields. The parrot cichlid swam freely in a transparent tank filled with still fresh water. The motion camera was placed below the tank. A mirror was placed on a side wall of the tank to enhance the intensity of backward scattered light received by the SDPIV camera. The viewing angle between the optical axis of each camera and the object plane norm was 30°.

is estimated to be less than 4.2% of the true values, and of out-of-plane velocity components less than 5.1% of the true values.

Measurements of kinematic parameters

To derive kinematic parameters pertaining to the average swimming velocity, body angle and sinking angle, we filmed and analyzed the motion of a forward-sinking parrot cichlid. The body angle (θ_b) is defined as the angle between the lateral midline of fish body and the horizontal (see Fig. 1A). The sinking angle is defined as the angle between the swimming direction and the horizontal. We filmed the fish motion with the two high-speed cameras used for SDPIV measurements. One camera filmed the fish motion from a side (i.e. lateral) view and the other from a top (i.e. dorsal) view. The recorded images of the side-view camera were analyzed using MotionPro X Studio software (IDT) to evaluate the kinematic parameters. The top-view camera served only for simultaneously monitoring the swimming path of the fish.

During the SDPIV experiment on a parasagittal plane, an additional motion camera (Sony HDR-SR1, 60 frames s^{-1}) was placed beneath the water tank (Fig. 2) to film simultaneously the fish motion. The body angle and sinking angle of the forward-sinking parrot cichlid were estimated from the SDPIV image sequences. The backward-mapping polynomials determined in the SDPIV calibration procedure served to correct for the perspective error associated with the swimming path and the body and sinking angles. Otherwise, for the SDPIV experiment on a transverse plane, the camera filmed the fish motion from an approximately side view; the average swimming velocity and body and sinking angles were estimated from these motion-camera images.

Quantitative estimation of forces

Temporally averaged locomotive forces were evaluated quantitatively based on a vortex-ring model (Drucker and Lauder, 1999; Drucker and Lauder, 2005; Nauen and Lauder, 2002a; Saffman, 1992; Spedding et al., 1984; Stamhuis and Nauwelaerts, 2005). The temporally averaged locomotive force (or central jet force) was calculated using:

$$\mathbf{F} = I_r/T_j = \rho A_r \Gamma / T_j ,$$

in which I_r is the fluid impulse, ρ is the density of water (1000 kg m^{-3} at 20°C), A_r is the ring area, Γ is the absolute mean value of the circulation of the vortex pair, and T_j is the interval during which the vortex ring (or jet) is generated. $\mathbf{F}$ is essentially an uncorrected jet force because the calculation is based on the two-dimensional in-plane velocity fields; to obtain the true jet force $\mathbf{F}_j$, the force $\mathbf{F}$ was further rectified using trigonometric relations between the mean velocity vector of the central jet and the plane of the light sheet. The mean velocity vector of the central jet was determined on averaging ten velocity vectors in the central jet region. To calculate the circulation Γ, we performed closed-loop integration (Saffman, 1992) along a path defined as the zero-vorticity boundary of a vorticity concentration of a vortex.

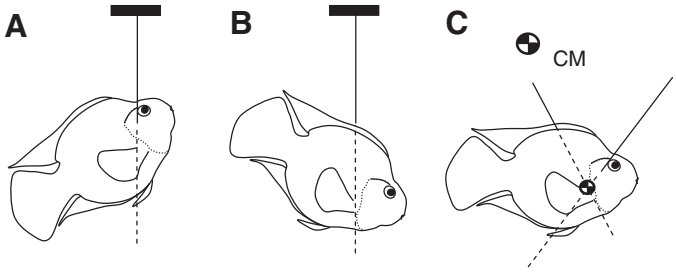

Fig. 3. Sketches showing the measurement of the center of mass. (A,B) An unconscious fish was carefully wrapped in nylon string and then suspended for photography; the procedure was repeated several times with the string in different positions each time. (C) The center of mass (CM; indicated by a black-and-white checked circle) was located by determining the intersection of any two extensions of the upright nylon strings from photographs.

Recognition of a vortex core

We identified the locations of vortex cores mainly by the method of the λ_2-value (second-largest eigenvalue of a symmetric tensor $S^2+\Omega^2$) that is a Galilean invariant (Haller, 2005; Jeong and Hussain, 1995). Within a flow field, regions of negative λ_2 belong to the vortex core area, and locations of zero λ_2 correspond to the boundary of the vortex core.

Measurement of the center of mass

To measure the center of mass of the fish body, we anaesthetized three parrot cichlids in advance using clove oil. We carefully tied a nylon string around the unconscious fish and then suspended it (Fig. 3) for photography. This procedure was repeated several times with the string in different positions each time (Fig. 3). After the measurements, the fish was released into a tank filled with fresh water to recover.

For a suspended fish, the extension of the upright nylon string definitely passed through the center of mass of the fish; accordingly we located the center of mass by determining the intersection of any two extensions of the upright nylon strings from photographs (Fig. 3C). The center of mass of a parrot cichlid is located approximately, in a lateral view, at a point near the dorsal tip of the pectoral fin base.

Measurement of the center of buoyancy

The same fish used to measure the center of mass were used for the center of buoyancy measurements. The parrot cichlid is

negatively buoyant because an anaesthetized parrot cichlid sinks when it is dropped into the water. The weight of the fish hence exceeds the buoyant force. Moreover, an anaesthetized parrot cichlid in the water has its belly upward, which indicates that the center of buoyancy is located at a point ventral to the center of mass.

We were unable to determine the exact location of the center of buoyancy, but found only a straight line on which the center of buoyancy is located. For a submerged body, the center of buoyancy is well known to be the center of geometry. As the fish apparently lacks a uniform density, we could not locate exactly the center of buoyancy by simply determining the center of geometry. We constructed a simple test section to find the desired straight line (Fig. 4A); the test section (a rectangular, transparent water container) was designed to be narrow (width ~9 cm), only slightly wider than the lateral body width of the parrot cichlid, thus preventing the sinking fish body from rolling (rotation about its longitudinal axis) and yawing (left–right rotation about the dorsal-ventral axis). The sinking fish was allowed only to pitch (rotation about the lateral axis of the body with head up or down).

On becoming unconscious, the anaesthetized fish was gently dropped into the test section (in a belly up and tilted position) and filmed. The sinking fish body tended initially to rotate (i.e. pitch), but it soon ceased rotating, which indicated that the centers of mass and buoyancy were then on the same vertical line (Weihs, 1993). To determine the straight line on which the center of buoyancy was located, we selected the recorded images for this non-rotating state of the fish body. On these selected images, the straight line was determined simply on drawing a vertical line passing through the center of mass of the fish body (Fig. 4B); this straight line approximately connected the center of mass and the base of the pelvic fin. This finding indicates that the centers of mass and of buoyancy occur approximately at the same relative longitudinal location of the fish body, so that the fish is normally neutral in a hydrostatic pitching equilibrium (Weihs, 1993). Although the exact location of the center of buoyancy is unknown, the center of buoyancy is definitely located aft of the center of mass in a forward-sinking parrot cichlid, because the fish adopts a tilted-down swimming posture, implying that the fish body is unstable in pitching.

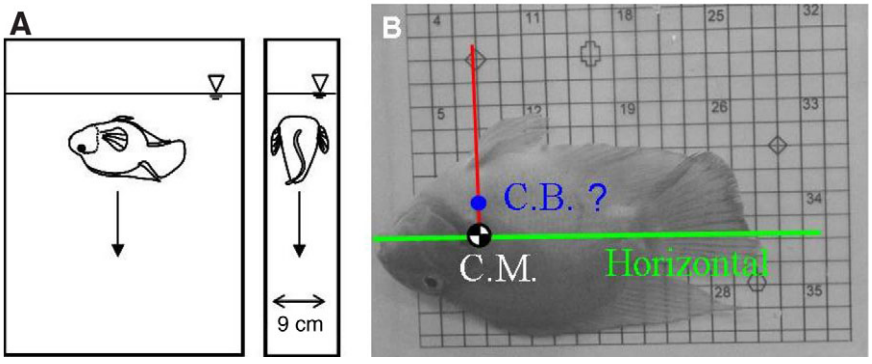

Fig. 4. Measurement of the center of buoyancy of a parrot cichlid. (A) To find the desired straight line on which the center of buoyancy was located, a fish in an unconscious state was dropped into a simple test section. The test section (a rectangular, transparent water container) was narrow (width ~9 cm), only slightly wider than the body of the parrot cichlid, so as to prevent the sinking fish from rolling and yawing and only allowing it to pitch. The sinking fish was filmed. (B) The straight line sought was simply determined on drawing a vertical line passing through the center of mass of a non-rotating fish body. This straight line (red) approximately connected the center of mass (CM) and the base of pelvic fin. CB, the center of buoyancy of the fish body, indicated by the blue filled circle.

RESULTS

Kinematic parameters

A forward-sinking parrot cichlid adopting a tilted-down swimming posture had a body angle in a range between 19° and 45° (25±5.9°, mean ± s.d., N=66). The sinking angle was in the range 10°–69° (33±13°, mean ± s.d., N=66). The average swimming velocity of the fish was in the range 0.011–0.11 m s^{-1} (0.051±0.027 m s^{-1}, mean ± s.d., N=66). The beat frequency of the caudal fin was in the range 0.9–2.2 Hz (1.4±0.36 Hz, mean ± s.d., N=66).

Flow fields and locomotive forces generated by CFP

We acquired in total of 120 SDPIV image sequences in the experiment, from which 65 sequences free of image occlusion were selected and analyzed to obtain flow velocity fields (13 sequences for the transverse plane and 52 sequences for the parasagittal plane).

In parrot cichlids a CFP during forward sinking generates propulsive forces involving a negative lift and thrust. The measured near-fin wake revealed that oscillating flow jets consisting of components oriented posteriorly (downstream), laterally and dorsally, designated here as CFP jets, were generated periodically with a caudal fin executing CFP. The dorsally propagating fin wave initially trapped a fluid mass and then accelerated it dorsally. For instance, Fig. 5 shows a representative sequence of four instantaneous flow fields (on a transverse plane) that demonstrate the near-fin wake associated with a CFP; the time was set to t=0 for Fig. 5A. Fig. 5A–D show phases at approximately 29, 50, 60 and 65%, respectively, of a tail beat cycle that was initiated when the dorsal part of the caudal fin was at the last right excursion. The in-plane velocity vectors (Fig. 5A) show two CFP jets (indicated with bold white arrows) that occur near the dorsal and ventral parts, respectively, of the caudal fin. The dorsal (upper) CFP jet was formed earlier than the ventral (lower) one. The dorsal CFP jet was approaching a state of being expelled. The fluid mass of the ventral CFP jet was initially trapped by the fin into a concave zone of low pressure that was created by the lateral movement of the ventral part of the caudal fin, according to the principle of conservation of mass.

Three vortices (designated with white *1*, *2* and *4*) were observed (Fig. 5A) adjacent to the dorsal and ventral CFP jets. The dorsal CFP jet was the central jet of the *1* and *2* vortex pair. At this instant, vortex *2* was structurally shared by the dorsal and ventral CFP jets. The lower part of vortex *2* overlapped spatially with the ventral CFP jet. In a three-dimensional aspect, the dorsal CFP jet is the central jet of a three-dimensional vortex ring; vortex pairs *1* and *2* adjacent to the dorsal CFP jet were part of the vortex loop of the vortex ring. The vortex loop pertaining to the dorsal CFP jet partly overlapped the ventral CFP jet.

In particular, vortex *2* did not subsequently continue to grow. The in-plane velocity vectors in Fig. 5B–D show that vortex *2* in Fig. 5A was destroyed and gradually weakened by a newly formed vortex *3* (in Fig. 5C). The formation of vortex *3* results from the reinforcement of the ventral CFP jet.

At t=0.16 s approximately (Fig. 5B), the dorsal CFP jet began to be expelled. The in-plane velocity magnitudes were smaller on average at the ventral CFP jet than at the dorsal CFP jet (Fig. 5A–D). The ventral CFP jet was

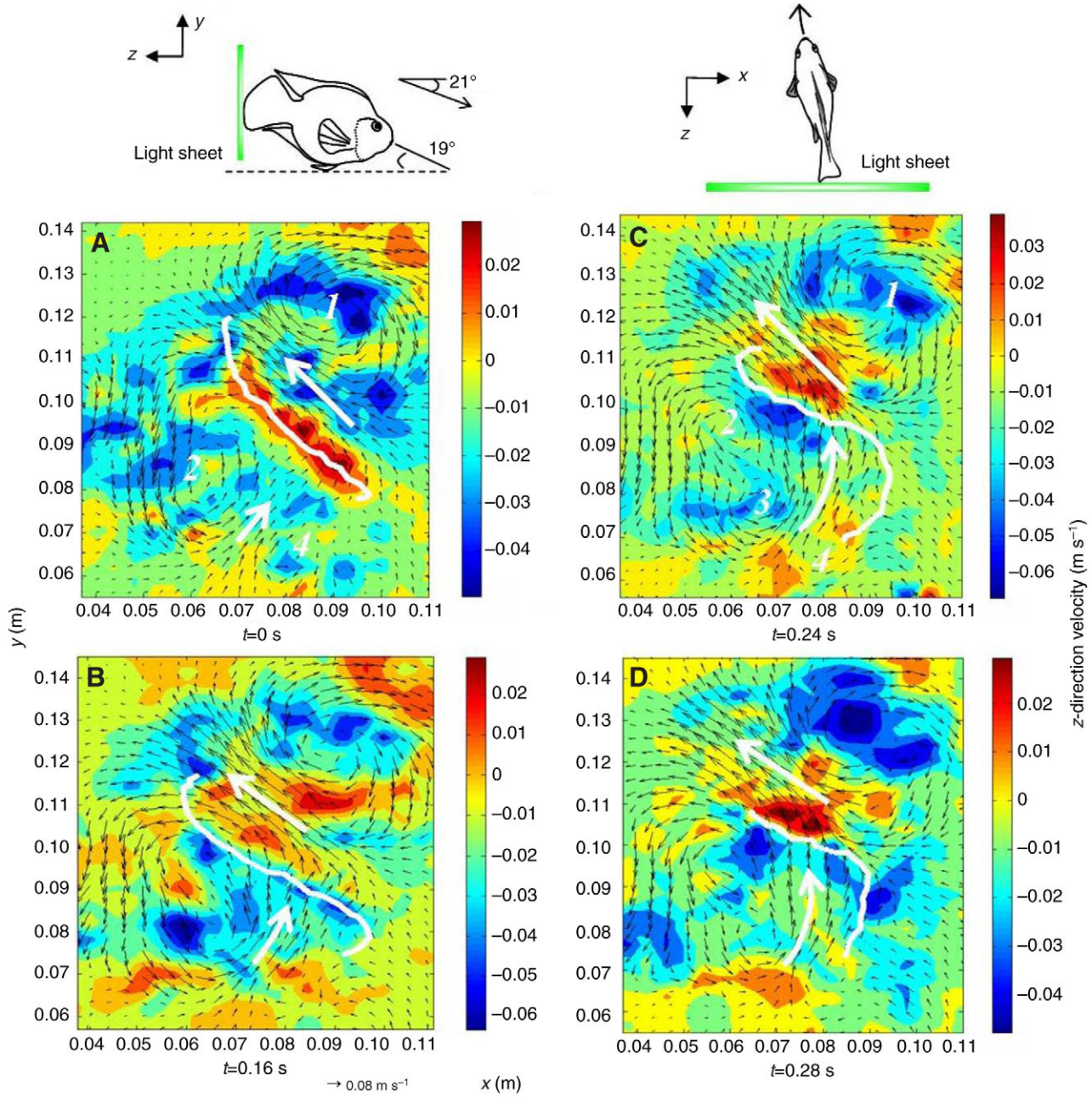

Fig. 5. Flow velocity fields of a selected swimming sequence measured on a transverse plane. The schematic drawings (not to scale) at the top of the figure illustrate lateral and dorsal views of a fish swimming (nearly steadily) across the light sheet during forward sinking. For the fish, the sinking angle was approximately 21°; the body angle was approximately 19°. The average swimming velocity of the fish was approximately 0.05 m s^{-1}; the beat frequency of the caudal fin was 1.3 Hz. The angle between the swimming direction and the *y*–*z* plane was approximately 28°. (A–D) The color contour represents the magnitude of z-direction velocity *W*, i.e. the out-of-plane velocity; the in-plane velocities are represented by black vectors. The bold white curves indicate the projection of the trailing edge of the caudal fin on the light-sheet plane. (A) The dorsal part of the caudal fin was beating toward the left side, and the ventral part toward the right side (at approximately 29% of a tail beat cycle that was initiated when the dorsal part of the caudal fin was at the last right excursion). (B) Both the dorsal and ventral parts of the caudal fin were decelerating and approaching their lateral beat excursions (at approximately 50% of the tail beat cycle). At approximately *t*=0.2 s, both the dorsal and ventral parts of the caudal fin attained their lateral beat excursions and began to beat toward the opposite side. (C) The accelerating dorsal and ventral parts of the caudal fin were beating toward the right and left sides respectively (at approximately 60% of the tail beat cycle). (D) Both the dorsal and ventral parts of the caudal fin were still accelerating (at approximately 65% of the tail beat cycle). The bold white arrows indicate the dorsal and ventral CFP jets that were generated by the caudal fin executing a caudal fin-wave propagation (CFP). White numbers (*1*–*4*) in A and C indicate vortices adjacent to CFP jets.

more dorsally oriented in Fig. 5D than in Fig. 5A, indicating that the caudal fin had imparted dorsally oriented momentum to the jet and correspondingly obtained a ventrally oriented reaction force. The ventral CFP jet eventually evolved into a dorsal CFP jet and became expelled, with a lateral component of orientation opposed to that of the dorsal CFP jet in Fig. 5.

The flow fields shown in Fig. 5 were not on an exactly transverse plane as an angle of approximately 28° existed between the

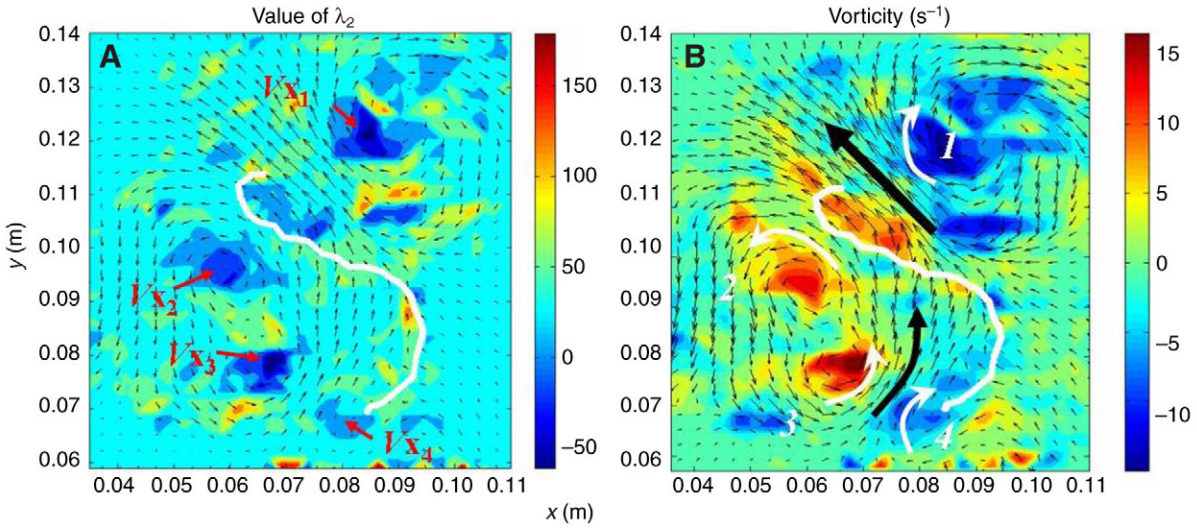

Fig. 6. Contours of λ_2-value and vorticity for the flow field shown in Fig. 5C. (A) λ_2-value contour; the locations designated *Vx*$_1$, *Vx*$_2$, *Vx*$_3$ and *Vx*$_4$ are cores of vortices adjacent to caudal fin-wave propagation (CFP) jets. (B) Vorticity contour; bold black arrows indicate the dorsal and ventral CFP jets located between counter-rotating vortex pairs. The white, curved bold arrows indicate the directions of rotation of four vortices adjacent to the dorsal and ventral CFP jets. The bold white curves (A,B) indicate the projection of the trailing edge of the caudal fin on the plane of the light sheet. The black vectors (A,B) indicate the in-plane flow velocities.

swimming direction of the fish and the *y*–*z* plane. This condition, however, did not affect the identification of the flow topology of the near-fin wake on a transverse plane. Our results indicate that alterations of the flow pattern of the near-fin wake were correlated mainly with the phases of the caudal-fin beat cycle.

The contours of the λ_2-value and vorticity corresponding to the velocity field in Fig. 5C are shown in Fig. 6. The locations designated *Vx*$_1$, *Vx*$_2$, *Vx*$_3$ and *Vx*$_4$ (Fig. 6A) are, respectively, vortex cores of vortices *1*, *2*, *3* and *4* (λ_2=–52.0, –37.9, –51.6, –2.29, respectively). The λ_2-value contour confirmed the identification and location of vortices *1*, *2*, *3* and *4*. The vorticity contour (Fig. 6B) confirmed the occurrence of CFP jets that were generated by the caudal fin because the intermediate region between a clockwise vortex (with negative vorticity) and a counterclockwise vortex (with positive vorticity) are recognizable as a jet flow. The two-dimensional in-plane flow pattern comprising a counter-rotating vortex pair and its central jet is essentially a vortex-ring-like structure three-dimensionally.

Fig. 7 shows the near-fin wake measured on a parasagittal (*x*–*y*) plane of the light sheet that was approximately parallel to, and overlapping, the middle plane of the fish body (see the schematic drawing at the top of Fig. 7). Fig. 7A and B are two instantaneous velocity fields within a stroke cycle. Fig. 7C and D are respectively the corresponding vorticity contours for Fig. 7A and B. For Fig. 7A and C, the dorsal part of the caudal fin was beating laterally toward the positive *z*-direction, while the ventral part of the caudal fin beat was toward the negative *z*-direction. The in-plane velocity vectors (Fig. 7A,C) reveal the dorsal and ventral CFP jets generated. The dorsal CFP jet was formed earlier than the ventral one. The dorsal CFP jet having posterodorsally oriented in-plane velocity components and positive *W* (out-of-plane) velocity components was being expelled near the dorsal part of the caudal fin (Fig. 7A,C). The ventral CFP jet, having anterodorsally oriented in-plane velocity components and negative *W* velocity components, was approximately in a stage of initial formation.

Three vortices (designated with white P_1, P_2 and P_3 in Fig. 7C) were observed (Fig. 7A,C) adjacent to the dorsal and ventral CFP jets. The dorsal CFP jet was the central jet of the vortex pair comprising vortices P_1 and P_2. The ventral CFP jet was the central jet of the vortex pair comprising vortices P_2 and P_3. Vortex P_2 was hence structurally shared by the dorsal and ventral CFP jets. From a three-dimensional aspect, the vortex loop pertaining to the dorsal CFP jet partly overlapped the ventral CFP jet.

In Fig. 7B,D, the dorsal part of the caudal fin was beating laterally toward the negative *z*-direction, while the ventral part of the caudal fin toward the positive *z*-direction. The ventral CFP jet observed in Fig. 7A,C was being expelled near the dorsal part of the caudal fin (Fig. 7B,D). The CFP jet (between vortices P_2 and P_3) comprised components oriented dorsally, posteriorly and laterally.

Table 1 presents the CFP jet forces calculated with flow data measured from the parasagittal (*x*–*y*) plane of the light sheet (cf. the schematic drawing at the top of Fig. 7). The circulation Γ used to calculate the jet force was taken as the average of absolute Γ for vortices P_1 and P_2 or vortex P_3 as the CFP jet was expelled. Both the mean vertical force ($\mathbf{F}_{jy}$) and lateral force ($\mathbf{F}_{jz}$) were approximately four times the mean horizontal force ($\mathbf{F}_{jx}$) (Table 1). The lateral forces would cancel each other because the caudal fin beat periodically and the CFP jets were oscillating laterally. In sum, the CFP in a forward-sinking parrot cichlid produces mainly a negative lift and a small thrust. As the caudal fin is located posterior to the center of mass of the fish body, the force generated *via* CFP can result in a head-up pitching moment that lifts up the fish head.

Flow fields and locomotive forces generated by pectoral fins

Within a complete stroke cycle, motions of the maneuvering pectoral fins of a forward-sinking parrot cichlid executing a CFP involved sequential fin movements of (1) anteroventrally oriented fin abduction (i.e. the down-stroke), (2) rotating and cupping the fin (i.e. stroke reversal) and (3) posterodorsally oriented fin adduction (i.e. the up-stroke). The results of the flow measurement reveal that the down-stroke of the pectoral fin created a fluid jet (designated a down-stroke jet) comprising components oriented posteriorly, laterally and ventrally (see Fig. 8). A head-down pitching moment was generated by the pectoral fins during the down-stroke. The up-stroke of the pectoral fin also created a fluid jet (designated

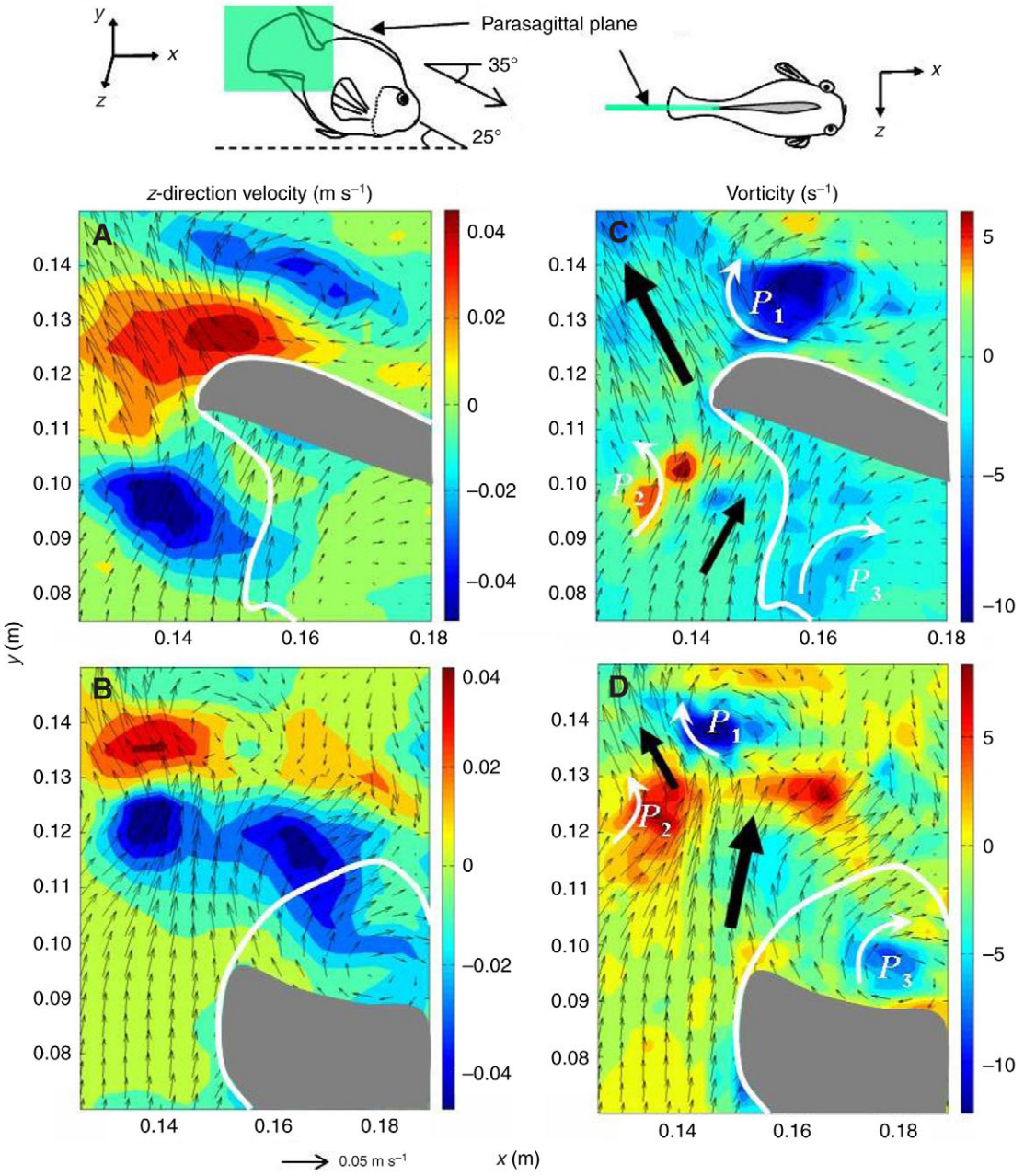

Fig. 7. Flow velocity fields and vorticity contours of the near-fin wake measured on a parasagittal (*x*–*y*) plane of the light sheet approximately parallel to, and overlapping, the middle plane of the fish body. The schematic drawings (not to scale) at the top of the figure illustrate the lateral and dorsal views of the swimming fish during forward sinking. For the fish, the sinking angle was approximately 35°; the body angle was approximately 25°. The average swimming velocity of the fish was approximately 0.053 m s^{-1}; the frequency of tail beating was 1.3 Hz. The interval between A and B was 0.376 s. (A–D) Black vectors represent the in-plane velocity; gray areas indicate zones of the light sheet that were shaded by the maneuvering caudal fin and were unobservable with the SDPIV cameras. (A,B) The color contour represents the magnitude of the *z*-direction velocity *W*. (C,D) Vorticity contours corresponding to velocity fields in A and B, respectively. The bold white curves indicate the projection of the trailing edge of the caudal fin on the plane of the light sheet. The bold black arrows indicate the dorsal and ventral caudal fin-wave propagation (CFP) jets generated by the caudal fin executing a CFP. White P_1, P_2 and P_3 denote vortices adjacent to the CFP jets; the white curved arrows indicate the directions of rotation of vortices P_1, P_2 and P_3.

an up-stroke jet) comprising components oriented posteriorly, laterally and ventrally.

Fig. 8 shows the wake of the pectoral fin measured on a parasagittal (*x*–*y*) plane of the light sheet approximately parallel to the fish body and intersecting the pectoral fin (see the schematic drawing at the top of Fig. 8). Fig. 8A–C are instantaneous velocity fields of the wake for down-stroke, stroke reversal and up-stroke, respectively, within a stroke cycle. Fig. 8D–F are the corresponding vorticity contours for Fig. 8A–C, respectively. Fig. 8A demonstrates that a three-dimensional down-stroke jet was created at the end of the down-stroke. A counter-rotating vortex pair (K_1 and K_2) adjacent to the down-stroke jet was observable from the in-plane velocity vectors and the vorticity contour (Fig. 8D). The in-plane component of the down-stroke jet indicates that a head-down pitching moment was induced because the pectoral fin was located posterior to the center of mass of the parrot cichlid during the down-stroke.

Table 1. Measurement of CFP jet forces

Parameter	Unit	Value
Duration of jet generation, T_j	s	0.40±0.05
Ring impulse, $I_r \times 10^4$	kg m s^{-1}	18.00±5.63
Uncorrected jet force, **F**	mN	4.6±1.1
True jet force, $\mathbf{F}_j$	mN	6.3±2.8
x-direction component of $\mathbf{F}_j$, $\mathbf{F}_{jx}$	mN	0.98±0.74
y-direction component of $\mathbf{F}_j$, $\mathbf{F}_{jy}$	mN	4.4±1.1
z-direction component of $\mathbf{F}_j$, $\mathbf{F}_{jz}$	mN	3.9±3.3
Mean jet-velocity magnitude	cm s^{-1}	4.76±0.76

Values are presented as means ± s.d.; *N*=12 for each parameter. Jet forces were calculated using flow data measured from the parasagittal plane. $\mathbf{F}_{jx}$ and $\mathbf{F}_{jz}$ are reported as absolute values. $\mathbf{F}_{jz}$ corresponds to the lateral force.

The mean swimming velocity of the fish was in a range of 0.043–0.069 m s^{-1}; the sinking angle was approximately 28–39°; the body angle was approximately 19–27°. The obtuse angle between the direction of the average swimming velocity of the fish and the mean in-plane jet orientation was approximately 115–160°.

Table 2. Measurement of pectoral-fin jet forces

Parameter	Unit	Down-stroke	Up-stroke
Duration of jet generation, T_j	s	0.28±0.05	0.24±0.03
Ring impulse, $I_r \times 10^4$	kg m s^{-1}	19.0±9.1	7.9±3.2
Uncorrected jet force, **F**	mN	6.8±2.9	3.3±1.4
True jet force, $\mathbf{F}_j$	mN	12.6±5.4	6.7±5.0
x-direction component of $\mathbf{F}_j$, $\mathbf{F}_{jx}$	mN	–0.79±0.75	–3.0±1.1
y-direction component of $\mathbf{F}_j$, $\mathbf{F}_{jy}$	mN	–6.7±2.9	1.1±1.1
z-direction component of $\mathbf{F}_j$, $\mathbf{F}_{jz}$	mN	10.6±4.7	5.7±5.0
Mean jet-velocity magnitude	cm s^{-1}	5.86±1.00	5.85±1.51

Values are presented as means ± s.d.; *N*=7 for each parameter. Jet forces were calculated using flow data measured from the parasagittal plane. The forces listed are per pectoral fin.

The mean swimming velocity of the fish was in a range 0.056–0.073 m s^{-1}; the sinking angle was approximately 25–35°; the body angle was approximately 19–28°. The acute angle between the horizontal and the orientation of the down-stroke in-plane jet was approximately 30–75° (beneath the horizontal). The acute angle between the horizontal and the orientation of up-stroke in-plane jet was approximately 0–30° (above the horizontal).

During stroke reversal, both the in-plane and out-of-plane velocity fields indicate that a new fluid jet was ready to form (Fig. 8B). The formation of a new vortex K_3 was initiated (Fig. 8E). The in-plane velocity vectors between vortices K_1, K_2 and K_3 formed a curved jet (represented by the bold curved black arrow in Fig. 8E).

Fig. 8C shows the upstroke jet formed at the end of the up-stroke. The up-stroke jet was more posteriorly oriented than the down-stroke jet. The in-plane component of the up-stroke jet passed approximately through the center of mass of the fish body; the pectoral fin was thus considered not to generate a pitching moment during an up-stroke. Vortices K_3 and K_2 with counter-rotating directions were the vortex pair adjacent to the up-stroke jet.

Table 2 presents the down-stroke and up-stroke jet forces calculated using flow data measured from the parasagittal (*x*–*y*) plane of the light sheet (cf. the schematic drawing at the top of Fig. 8). The circulation Γ used in the jet force calculation was taken as an average of absolute Γ for vortices K_1 and K_2 at the end of the down-stroke, and the average of absolute Γ for vortices K_2 and K_3 at the end of the up-stroke. The total jet forces of the down-stroke were approximately twice as large as that of the up-stroke. Both down-stroke and up-stroke produced large lateral forces (F_{jz}). The up-stroke produced a considerable thrust and a small negative lift. The thrust produced by an up-stroke was larger than that produced by a down-stroke.

DISCUSSION

Pitching stabilization *via* CFP

The experimental results indicate that the main function of the caudal fin executing CFP is to induce a head-up pitching moment that can stabilize the fish body in pitching. Fluid jets generated by the caudal and pectoral fins of a forward-sinking parrot cichlid are summarized in Fig. 9. The dorsally propagating wave of the caudal fin results in the generation of CFP jets – oscillating fluid jets comprising components oriented posteriorly, laterally and dorsally. During the down-stroke, the pectoral fin sheds a fluid jet (i.e. the down-stroke jet) comprising components oriented posteriorly, laterally and ventrally (Fig. 9). During the up-stroke, the pectoral fin also sheds a fluid jet (i.e. the up-stroke jet) comprising components oriented posteriorly, laterally and ventrally (Fig. 9). The down-stroke jets were more ventrally oriented than the up-stroke jets. The hydrodynamic forces obtained by the fish are oriented in a direction opposite that of the fluid jets, in accordance with Newton's third law.

For a forward-sinking parrot cichlid, the fish body should be inherently unstable because the buoyant force (see $\mathbf{F}_B$ in Fig. 10) induces a head-down pitching moment (cf. M_B in Fig. 10). The down-stroke force (see $\mathbf{F}_{PFD}$ in Fig. 10) of the pectoral fin also induces a head-down pitching moment (see M_{PF} in Fig. 10) as it was applied posterior to the center of mass. To prevent the fish from rotating (i.e. pitching) and to achieve a stable swimming posture, an adequate head-up pitching moment should be applied on the fish body (Webb, 2002; Webb, 2004; Weihs, 1993). Our experimental results indicate that the caudal fin executing a CFP can generate CFP forces (see the $\mathbf{F}_{CFP}$ in Fig. 10) that induce a head-up pitching moment. As the swimming posture of the fish is stable, one can reasonably infer that those head-down pitching moments that destabilize the fish body are balanced approximately by the head-up pitching moment induced from a CFP (see Fig. 10). The behavior of a CFP functionally facilitates the pitching stabilization in a forward-sinking parrot cichlid that adopts a tilted-down swimming posture.

During forward rising, a parrot cichlid is observed to adopt a tilted-up swimming posture with the head up and tail down. In this tilted-up posture, the center of buoyancy is located fore of the center of mass. The fish body is inherently unstable also in pitching as the buoyant force induces a destabilizing head-up pitching moment. We observed that the caudal fin wave of a forward-rising parrot cichlid propagates ventrally. One reasonably infers that, to facilitate the pitching stabilization, the force generated by the ventrally propagating caudal fin wave is dorsally oriented and induces a head-down pitching moment.

For a parrot cichlid, the magnitude of the buoyant force is typically larger than that of the hydrodynamic forces generated by a fish's caudal and pectoral fins (the buoyant force of a fish is estimated roughly as the weight of water displaced by a submerged fish, in a graduated measuring cup). The moment arm associated with the buoyant force is hence much shorter than those associated with the CFP force or the down-stroke force of pectoral fins. For instance, the buoyant force of a parrot cichlid used in this work is approximately 1.6 N, but the hydrodynamic forces generated by a fish's fins are in a range approximately 1–10 mN (cf. Tables 1 and 2). To balance all the induced pitching moment, the magnitude of

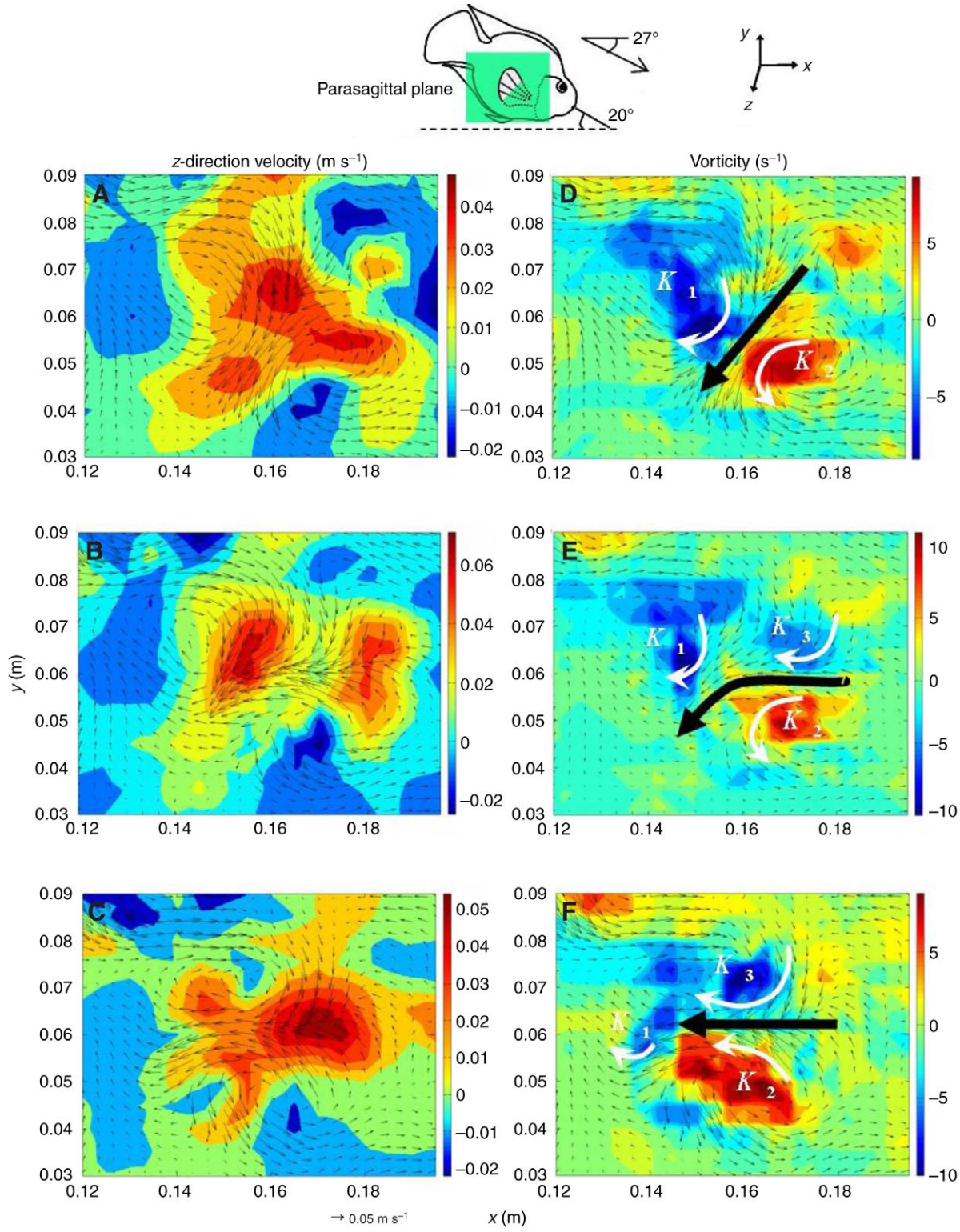

Fig. 8. Wake of the pectoral fin measured on a parasagittal (*x*–*y*) plane of the light sheet approximately parallel with the fish body and intersecting the pectoral fin. The schematic drawing (not to scale) at the top of the figure shows a lateral view of a swimming fish during forward sinking. The average swimming velocity of the fish was approximately 0.066 m s^{-1}; the sinking angle was approximately 27°; the body angle was approximately 20°. (A–C) Instantaneous velocity fields of the wake for the down-stroke, stroke reversal and up-stroke, respectively. The time was set to *t*=0 s for A; (B) *t*=0.064 s; (C) *t*=0.224 s. The black vectors represent the in-plane velocity in A–D. The color contour represents the magnitude of the *z*-direction velocity *W* in A–C. (D–F) Vorticity contours corresponding to the velocity fields in A–C, respectively. The bold black arrows indicate the fluid jets generated by the pectoral fin. White K_1, K_2 and K_3 denote vortices adjacent to the down-stroke and up-stroke jets. The white and curved arrows indicate the directions of rotation of vortices K_1, K_2 and K_3. A three-dimensional down-stroke jet (A) and an up-stroke jet (C) were observed.

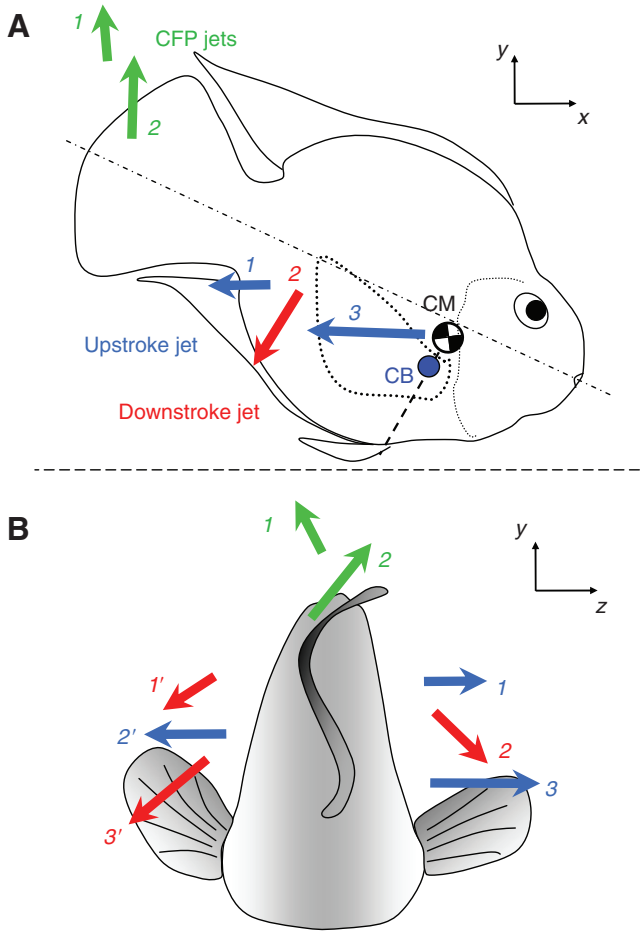

Fig. 9. Schematic drawings (not to scale) that illustrate the fluid jets generated by a caudal fin-wave propagation (CFP) and the pectoral fins in a forward-sinking parrot cichlid executing a CFP. (A) Lateral view, with the CFP, down-stroke and up-stroke jets indicated by green, red and blue arrows, respectively. CM, center of mass of the fish body, indicated by a white and black checked circle; CB, center of buoyancy of the fish body, indicated by a blue filled circle. The straight line connecting the CM and the CB is shown (dashed line). (B) CFP, down-stroke and up-stroke jets observed from behind the fish. The colored numbers adjacent to the jets denote the temporal order of formation of the jets in A and B; only the expelled CFP jets are displayed.

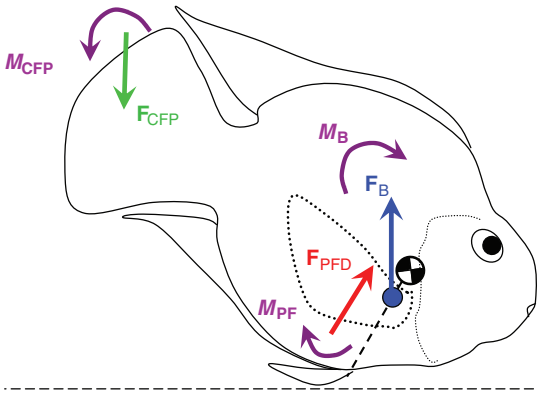

Fig. 10. Schematic drawing (not to scale) that illustrates the pitching-moment balance in a forward-sinking parrot cichlid adopting a tilted-down swimming posture. The caudal fin wave of the parrot cichlid propagates dorsally. The purple curved thick arrows represent the induced pitching moment. M_B is the head-down pitching moment induced by the buoyant force ($\mathbf{F}_B$). M_{PF} is the head-down pitching moment induced by the down-stroke force ($\mathbf{F}_{PFD}$) of the pectoral fin; M_{CFP} is the head-up pitching moment induced by the caudal fin-wave propagation force ($\mathbf{F}_{CFP}$). The behavior of a CFP functionally facilitates the pitching stabilization.

the head-down pitching moment induced by the buoyant force should be comparable with that of the hydrodynamic forces generated by a fish's fins. As the center of buoyancy is known to be located on a straight line connecting the center of mass and the base of the pelvic fin (see Fig. 4), one can further infer that the center of buoyancy is located at a point (on the straight line) near the center of mass.

The functional characteristics of CFP behavior might provide useful insight into the locomotive function of highly flexible or deformable appendages of aquatic animals, and would be also beneficial for the design of autonomous underwater vehicles with regard to control of pitching stability.

Structural characteristics of the CFP wake

Fig. 11 shows sequential two-dimensional schematic drawings that summarize the formation and evolution of CFP jets and vortices observable in the near-fin wake of a forward-sinking fish executing CFP; these CFP jets are three-dimensional (cf. Fig. 12). The flow patterns of the near-fin wake shown in Fig. 11A–D correspond to those observed at approximately the 1/3, 1/2, 4/5 and end phases, respectively, of a single CFP beat cycle. Alterations of the flow pattern of the near-fin wake are correlated mainly with the phases of the beat cycle of the caudal fin.

When observed from behind the fish (Fig. 11), the formation and evolution of a developing CFP jet can be divided approximately into three stages. A CFP jet is induced (or trapped) initially by a zone of low pressure created by the fin movement near the ventral part of the caudal fin (see Jet 2 in Fig. 11A). In this stage, the developing CFP jet orients approximately toward the direction of movement of the ventral part of the caudal fin. A CFP jet (see Jet 1 in Fig. 11A) formed earlier is expelled near the dorsal part of the caudal fin. Afterwards, the propagating fin wave gradually reorients and accelerates the developing CFP jet (Jet 2 in Fig. 11B,C). The caudal fin continuously imparts momentum to the fluid while the fin wave travels dorsally. In the second stage, the CFP jet formed earlier is almost completely expelled (Jet 1 in Fig. 11B), and the formation of a new CFP jet is initiated (Jet 3 in Fig. 11C).

In the third stage, the developing CFP jet eventually becomes a strong flow jet and is completely expelled near the dorsal part of the caudal fin (Jet 2 in Fig. 11D). In brief, a CFP jet, for example Jet 2 in Fig. 11, is initially induced (or trapped) by the ventral part of the caudal fin, subsequently strengthened and reoriented by the propagating fin wave, and eventually expelled near the dorsal part of the caudal fin.

We propose three-dimensional structures of the near-fin and far-fin wake of the CFP (see Fig. 12A,B). The three-dimensional near-fin wake presented in Fig. 12A structurally corresponds to the two-dimensional case shown in Fig. 11B. The far-fin wake (Fig. 12B) comprising linked vortex rings and oscillating central CFP jets strongly resembles a 'reverse von Karman vortex street' that is observable in the wake of carangiform swimmers or biomimetic foils (Lugt, 1995; Nauen and Lauder, 2002a; Nauen and Lauder, 2002b; Triantafyllou et al., 2000; Triantafyllou et al., 2004). The two-dimensional sketch at the upper right of Fig. 12B illustrates the vortex filaments of the far-fin wake observed on a parasagittal plane.

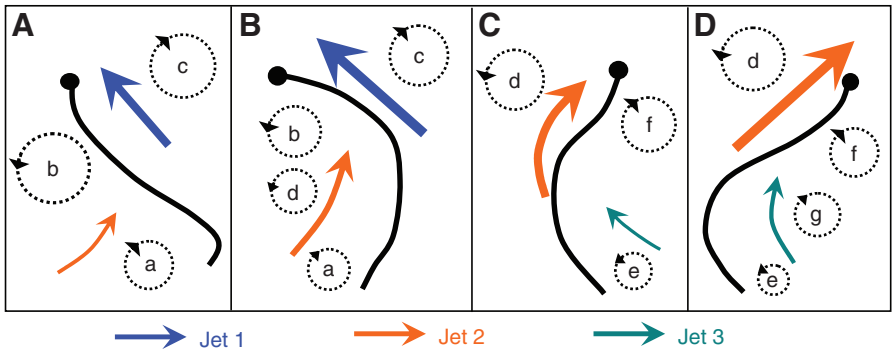

Fig. 11. Sequential two-dimensional schematic drawings (not to scale) summarizing the formation of a near-fin wake and the evolution of caudal fin-wave propagation (CFP) jets observable in a forward-sinking fish executing a CFP. These drawings pertain to observations made from behind the fish. (A–D) Flow patterns observed at approximately the 1/3, 1/2, 4/5 and end phases, respectively, of a CFP beat cycle. The black bold lines represent the trailing edge of the caudal fin; the black filled circle represents the dorsal tip. The colored arrows indicate CFP jets (designated Jet 1, Jet 2 and Jet 3) generated by the caudal fin. The dashed circles with arrows represent vortices (denoted a–g) adjacent to the CFP jet. The temporal order of formation is Jet 1, Jet 2 and then Jet 3.

We observed that an expelled CFP jet had a slightly divergent configuration. The dorsally propagating fin wave was initiated by the lateral movement of the ventral part of the caudal fin, which could first trap the fluid volume of a CFP jet and then expel it. The volume of the ventral CFP jet observed in Fig. 7A is divisible into approximately two parts: one, the right part, was nearer the ventral region of the caudal fin (or vortex P_3), whereas the other, the left part, was more distant from the ventral region of the caudal fin and nearer vortex P_2. The right part was directly accelerated by the fin displacement, whereas the left part was indirectly accelerated due to the fluid viscosity. While the ventral CFP jet was developing, the left part was expelled (or ejected) earlier than the right part, because the left part was farther from the caudal fin and hence left the influence of the caudal fin earlier. The left part would convect downstream according to its fluid inertia. The right part having not been expelled would be further propelled dorsally by the dorsally propagating fin wave, and become expelled eventually near the dorsal edge of the caudal fin. The in-plane velocity vectors (Fig. 7B) indicate the right part is more dorsally oriented than the left part, as the right part is dorsally propelled by the caudal fin for a greater duration. The CFP jet consequently showed a slightly divergent configuration as it was completely expelled (Fig. 7B).

A slightly divergent CFP jet is considered to be structurally similar to a split jet generated by the shark tail possessing an asymmetric shape (Wilga and Lauder, 2004). A split jet corresponds to a 'ring-within-a-ring' structure in the wake and is proposed to increase the vertical maneuverability of a shark (Wilga and Lauder, 2004). We infer that the slightly divergent CFP jet may also have a similar function of increasing the maneuverability. The CFP jet force may be adjustable by tuning separately the orientation of the two divergent parts (or components) of the jet.

Based on qualitative estimation, we found the volume of a CFP jet was generally increased when it was expelled. For the 'in-plane' aspect of flow fields (e.g. Fig. 7A,B), the volume variation of a CFP jet can be qualitatively estimated from an examination of the variation of the distance between the cores of vortex pairs of the CFP jet recognized by the λ_2-value (Jeong and Hussain, 1995). As this distance invariably increased, in the in-plane aspect the volume of a CFP jet increased when it was expelled. Otherwise, for the 'out-of-plane' aspect, the variation in volume of a CFP jet can be qualitatively estimated from an examination of the variation of the 'in-plane' area subject to negative W velocity (i.e. the out-of-plane velocity). As this area invariably increased, in the out-of-plane aspect the volume of a CFP jet increased when it was expelled. We consider

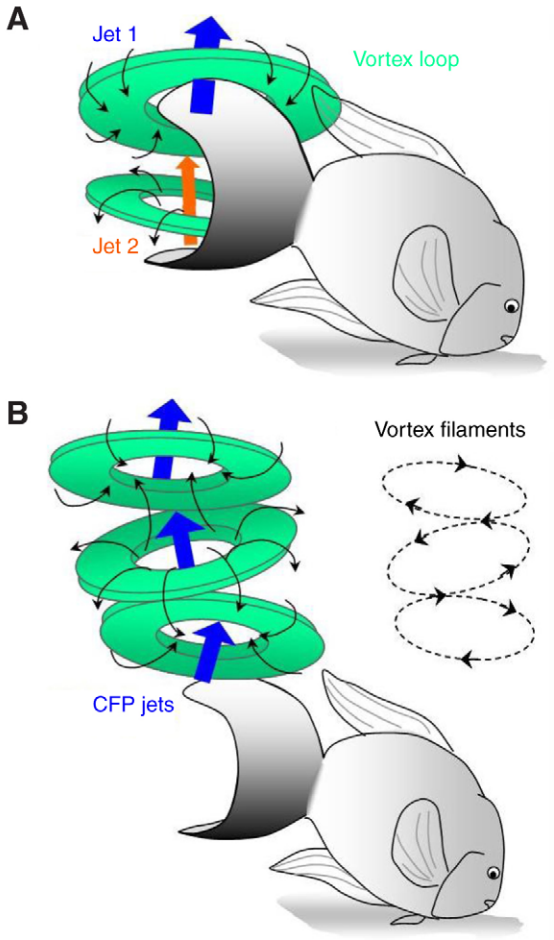

Fig. 12. Three-dimensional sketches that illustrate the proposed (A) near-fin and (B) far-fin wake of the caudal fin-wave propagation (CFP). The curved black arrows indicate the direction of vortex rotation. (B) The two-dimensional sketch at the upper right illustrates the vortex filaments of the far-fin wake observed on a parasagittal plane. Dashed lines and arrows indicate the vortex filaments and their directions. The feature of the slightly divergent configuration of a CFP jet is not illustrated here.

that the gradually increasing transverse amplitudes of the caudal fin wave gradually enlarge the fluid volume of a developing CFP jet due to gradually enlarged extent of interaction between fin and fluid.

In this work we also noticed that the motion of a CFP probably enabled the fish to recycle the energy imparted from a self-shed vortex. This is because the vortex or vortex loop pertaining to the dorsal CFP jet is spatially near, or even overlaps, the ventral CFP jet that has approximately the same velocity direction as the local vortex motion. Flow fields measured from both the transverse (Fig. 5) and parasagittal (Fig. 7) planes showed that the vortex loop pertaining to the dorsal CFP jet partly overlapped, or was near, the ventral CFP jet. The vortex loop of the dorsal CFP jet in Fig. 5 involved out-of-plane flows (with negative W velocity) that overlapped the ventral CFP jet; the counterclockwise circulatory flow of vortex *2* in Fig. 5 also partly overlapped the ventral CFP jet in the in-plane aspect. Vortex P_2 in Fig. 7C was structurally shared by the dorsal and ventral CFP jets. The schematic drawing in Fig. 11A illustrates that a vortex b is structurally shared by the dorsal and ventral jets (i.e. the Jet 1 and Jet 2). The circulation of a vortex or vortex loop theoretically indicates a flow angular momentum that can drive (because of fluid viscosity) nearby fluid mass flowing in the same direction of rotation of the vortex or vortex loop (Munson et al., 1998). The shed vortex (or vortex loop) pertaining to a dorsal CFP jet evidently assists the trapping of the fluid mass of the subsequently developing ventral CFP jet (Fig. 5). Since the energy (or momentum) involved in the circulation of the shed vortex was imparted by the fish, the energy was thus probably recycled on trapping the fluid mass, which is functionally similar to the vortex-based extraction of energy by aquatic animals that extracts energy from environmental vortices (Allen and Smits, 2001; Dabiri, 2007; Liao et al., 2003).

Functions of the pectoral fins

During an up-stroke, the pectoral fins generate considerable thrust and a small negative lift (cf. Table 2). Because the pectoral fins generate no pitching moment during an up-stroke, it is thought that the principal function of an up-stroke of a pectoral fin is to provide thrust, but the pectoral fin generates a head-down pitching moment during a down-stroke. This head-down pitching moment is detrimental to the pitching stability of a fish body as it cannot counteract the head-down pitching moment induced at the center of buoyancy. In summary, the pectoral fin of the parrot cichlid destabilizes the fish body in the aspect of pitching.

The lateral forces generated by pectoral fins are large (cf. Table 2), and are considered capable of stabilizing the fish body and preventing it from rolling, as reported previously (Drucker and Lauder, 1999). The lateral forces would approximately cancel, considering contributions of pectoral fins at both sides.

LIST OF ABBREVIATIONS

A_r	area of the vortex ring
CFP	caudal fin-wave propagation
DPIV	digital particle-image velocimetry
$\mathbf{F}$	uncorrected two-dimensional temporally averaged central jet force
$\mathbf{F}_B$	buoyant force
$\mathbf{F}_{CFP}$	the force generated by CFP
$\mathbf{F}_j$	true jet force
$\mathbf{F}_{jx}$	component of F_j in the x-direction
$\mathbf{F}_{jy}$	component of F_j in the y-direction
$\mathbf{F}_{jz}$	component of F_j in the z-direction
$\mathbf{F}_{PFD}$	down-stroke force of pectoral fin
I_r	fluid impulse
K_i	notation of vortices; i=1–3.
M_B	pitching moment generated by center of buoyancy
M_{CFP}	pitching moment generated by CFP
M_{PF}	pitching moment generated by the pectoral fin
P_i	notation of vortices; i=1–3.
S	symmetric part of the velocity gradient tensor
SDPIV	stereoscopic digital particle-image velocimetry
T	approximate period of the fin beat
T_j	interval over which force is generated
$T_{1–12}$	time steps
Vx_i	vortex core; i=1–4.
λ_2	second-largest eigenvalue of a symmetric tensor $S^2+\Omega^2$
ρ	density of water
Γ	absolute mean value of the circulation of the vortex pair
Ω	antisymmetric part of the velocity gradient tensor
θ_b	body angle
U, V, W	the in-plane and out-of-plane fluid velocities within the laser light sheet

The National Science Council of the Republic of China partially supported this work under contract numbers NSC 94-2218-E-007-056 and NSC 95-2218-E-007-026. We thank two anonymous reviewers for their constructive comments and advice on this paper. We also thank Yu-Chun Lin and Chung-Yi Li for discussion of the flow fields.

REFERENCES

Allen, J. J. and Smits, A. J. (2001). Energy harvesting eel. *J. Fluids Struct.* **15**, 629-640.
Dabiri, J. O. (2007). Renewable fluid dynamic energy derived from aquatic animal locomotion. *Bioinspir. Biomim.* **2**, L1-L3.
Drucker, E. G. and Lauder, G. V. (1999). Locomotor forces on a swimming fish: three-dimensional vortex wake dynamics quantified using digital particle image velocimetry. *J. Exp. Biol.* **202**, 2393-2412.
Drucker, E. G. and Lauder, G. V. (2000). A hydrodynamic analysis of fish swimming speed: wake structure and locomotor force in slow and fast labriform swimmers. *J. Exp. Biol.* **203**, 2379-2393.
Drucker, E. G. and Lauder, G. V. (2001). Wake dynamics and fluid forces of turning maneuvers in sunfish. *J. Exp. Biol.* **204**, 431-442.
Drucker, E. G. and Lauder, G. V. (2003). Function of pectoral fins in rainbow trout: behavioral repertoire and hydrodynamic forces. *J. Exp. Biol.* **206**, 813-826.
Drucker, E. G. and Lauder, G. V. (2005). Locomotor function of the dorsal fin in rainbow trout: kinematic patterns and hydrodynamic forces. *J. Exp. Biol.* **208**, 4479-4494.
Fish, F. E. and Lauder, G. V. (2006). Passive and active flow control by swimming fish and mammals. *Annu. Rev. Fluid Mech.* **38**, 193-224.
Gibb, A. C., Dickson, K. A. and Lauder, G. V. (1999). Tail kinematics of the chub mackerel *Scomber japonicus*: testing the homocercal tail model of fish propulsion. *J. Exp. Biol.* **202**, 2433-2447.
Haller, G. (2005). An objective definition of a vortex. *J. Fluid Mech.* **525**, 1-26.
Jeong, J. and Hussain, F. (1995). On the identification of a vortex. *J. Fluid Mech.* **285**, 69-94.
Lauder, G. V. (2000). Function of the caudal fin during locomotion in fishes: kinematics, flow visualization, and evolutionary patterns. *Am. Zool.* **40**, 101-122.
Lauder, G. V. and Drucker, E. (2002). Forces, fishes and fluids: hydrodynamic mechanisms of aquatic locomotion. *News Physiol. Sci.* **17**, 235-240.
Lawson, N. J. and Wu, J. (1997). Three-dimensional particle image velocimetry: experimental error analysis of a digital angular stereoscopic system. *Meas. Sci. Technol.* **8**, 1455-1464.
Lecerf, A., Renou, B., Allano, D., Boukhalfa, A. and Trinite, M. (1999). Stereoscopic PIV: validation and application to an isotropic turbulent flow. *Exp. Fluids* **26**, 107-115.
Liao, J. and Lauder, G. V. (2000). Function of the heterocercal tail in white sturgeon: flow visualization during steady swimming and vertical maneuvering. *J. Exp. Biol.* **203**, 3585-3594.
Liao, J. C., Beal, D. N., Lauder, G. V. and Triantafyllou, M. S. (2003). Fish exploiting vortices decrease muscle activity. *Science* **302**, 1566-1569.
Lugt, H. J. (1995). *Vortex Flow in Nature and Technology.* Florida: Krieger.
Müller, U. K. and van Leeuwen, J. L. (2006). Undulatory fish swimming: from muscle to flow. *Fish Fish.* **7**, 84-103.
Müller, U. K., Van Den Heuvel, B. L. E., Stamhuis, E. J. and Videler, J. J. (1997). Fish foot prints: morphology and energetics of the wake behind a continuously swimming mullet (*Chelon labrosus* Risso). *J. Exp. Biol.* **200**, 2893-2906.
Munson, B. R., Young, D. F. and Okiishi, T. H. (1998). *Fundamentals of Fluid Mechanics.* New York: Wiley.
Nauen, J. C. and Lauder, G. V. (2002a). Hydrodynamics of caudal fin locomotion by chub mackerel, *Scomber japonicus*. *J. Exp. Biol.* **205**, 1709-1724.
Nauen, J. C. and Lauder, G. V. (2002b). Quantification of the wake of rainbow trout (*Oncorhynchus mykiss*) using three-dimensional stereoscopic digital particle image velocimetry. *J. Exp. Biol.* **205**, 3271-3279.
Prasad, A. K. (2000). Stereoscopic particle image velocimetry. *Exp. Fluids* **29**, 103-116.
Raffel, M., Willert, C. E., Wereley, S. T. and Kompenhans, J. (2007). *Particle Image Velocimetry: A Practical Guide.* New York: Springer.

Ramamurti, R., Sandberg, W. C., Löhner, R., Walker, J. A. and Westneat, M. W. (2002). Fluid dynamics of flapping aquatic flight in the bird wrasse: 3-D unsteady computations with fin deformation. *J. Exp. Biol.* **205**, 2997-3008.
Saffman, P. G. (1992). *Vortex Dynamics*. Cambridge: Cambridge University Press.
Sakakibara, J., Nakagawa, M. and Yoshida, M. (2004). Stereo-PIV study of flow around a maneuvering fish. *Exp. Fluids* **36**, 282-293.
Spedding, G. R., Rayner, J. M. V. and Pennycuick, C. J. (1984). Momentum and energy in the wake of a pigeon (*Columba Livia*) in slow flight. *J. Exp. Biol.* **111**, 81-102.
Stamhuis, E. J. and Nauwelaerts, S. (2005). Propulsive force calculations in swimming frogs. II. Application of a vortex ring model to DPIV data. *J. Exp. Biol.* **208**, 1445-1451.
Stamhuis, E. J. and Videler, J. J. (1995). Quantitative flow analysis around aquatic animals using laser sheet particle image velocimetry. *J. Exp. Biol.* **198**, 283-294.
Triantafyllou, M. S., Triantafyllou, G. S. and Yue, D. K. P. (2000). Hydrodynamics of fishlike swimming. *Annu. Rev. Fluid Mech.* **32**, 33-53.
Triantafyllou, M. S., Techet, A. H. and Hover, F. S. (2004). Review of experimental work in biomimetic foils. *IEEE J. Oceanic Eng.* **29**, 585-594.
Tytell, E. D. (2006). Median fin function in bluegill sunfish *Lepomis macrochirus*: streamwise vortex structure during steady swimming. *J. Exp. Biol.* **209**, 1516-1534.
Tytell, E. D. and Lauder, G. V. (2004). The hydrodynamics of eel swimming. I. Wake structure. *J. Exp. Biol.* **207**, 1825-1841.
Tytell, E. D., Standen, E. M. and Lauder, G. V. (2008). Escaping flatland: three-dimensional kinematics and hydrodynamics of median fins in fishes. *J. Exp. Biol.* **211**, 187-195.
Walker, J. A. and Westneat, M. W. (1997). Labriform propulsion in fishes: kinematics of flapping aquatic flight in the bird wrasse *Gomphosus varius* (Labridae). *J. Exp. Biol.* **200**, 1549-1569.
Walker, J. A. and Westneat, M. W. (2002). Kinematics, dynamics, and energetics of rowing and flapping propulsion in fishes. *Integr. Comp. Biol.* **42**, 1032-1043.
Webb, P. W. (2002). Control of posture, depth, and swimming trajectories of fishes. *Integr. Comp. Biol.* **42**, 94-101.
Webb, P. W. (2004). Maneuverability – general issues. *IEEE J. Oceanic Eng.* **29**, 547-555.
Weihs, D. (1993). Stability of aquatic animal locomotion. In *Fluid Dynamics in Biology* (ed. A. Y. Cheer and C. P. Van Dam), pp. 443-461. Providence, RI: American Mathematical Society.
Westerweel, J. and Van Oord, J. (1999). Stereoscopic PIV measurements in a turbulent boundary layer. In *Particle Image Velocimetry: Progress Towards Industrial Application* (ed. M. Stanislas, J. Kompenhans and J. Westerweel), pp. 459-478. Dordrecht Netherlands: Kluwer.
Wilga, C. D. and Lauder, G. V. (2002). Function of the heterocercal tail in sharks: quantitative wake dynamics during steady horizontal swimming and vertical maneuvering. *J. Exp. Biol.* **203**, 2261-2278.
Wilga, C. D. and Lauder, G. V. (2004). Hydrodynamic function of the shark's tail. *Nature* **430**, 850.
Willert, C. (1997). Stereoscopic digital particle image velocimetry for application in wind tunnel flows. *Meas. Sci. Technol.* **8**, 1465-1479.
Wolfgang, M. J., Anderson, J. M., Grosenbaugh, M. A., Yue, D. K. P. and Triantafyllou, M. S. (1999). Near-body flow dynamics in swimming fish. *J. Exp. Biol.* **202**, 2303-2327.